Journal of Geoscience and Environment Protection, 2026, 14(3), 81-98
https://www.scirp.org/journal/gep
ISSN Online: 2327-4344
ISSN Print: 2327-4336

Hydroclimatic Impacts of Volcanic Eruptions across Africa: An Aridity Index Perspective

Martha Adongo Obuo[1], Genesis Magara[2*], Tainyu Wang[1], Clara Liapapa[1], Abraham Okrah[2]

[1]School of Atmospheric Science, Nanjing University of Information Science & Technology, Nanjing, China
[2]School of Ecology and Applied Meteorology, Nanjing University of Information Science & Technology, Nanjing, China
Email: adongomartha60@gmail.com, *magaragenesis@gmail.com, wangtianyu2023@foxmail.com, claraliaps@gmail.com, okrahabraham2014@gmail.com

How to cite this paper: Obuo, M. A., Magara, G., Wang, T. Y., Liapapa, C., & Okrah, A. (2026). Hydroclimatic Impacts of Volcanic Eruptions across Africa: An Aridity Index Perspective. *Journal of Geoscience and Environment Protection, 14,* 81-98.
https://doi.org/10.4236/gep.2026.143004

Received: January 27, 2026
Accepted: March 3, 2026
Published: March 6, 2026

Abstract

Volcanic eruptions are an important driver of hydroclimate variability over Africa, yet their continent-wide impacts on aridity have not been systematically quantified. Using simulations of the Community Earth System Model Last Millennium Ensemble (CESM-LME), this study investigates the impacts of volcanic eruptions on the African aridity based on an aridity index (AI), defined as the ratio of precipitation to potential evapotranspiration (PET). Results reveal that aridity responses depend on both the season and the volcanic eruption latitude. Drying tends to occur within the climatological rainy-season band, and its position is further modulated by eruption latitude: Northern Hemisphere eruptions shift the main drying zone northward, whereas Southern Hemisphere eruptions shift it southward. Across all eruption events, soil moisture and surface runoff anomalies broadly agree with AI changes. The decomposition of AI anomalies reveals that precipitation reduction, which primarily results from circulation-driven reductions in horizontal and vertical moisture advection, dominates the drying, whereas PET plays a secondary role. These results provide a physical basis for improving predictions of African aridity following volcanic eruptions.

Keywords

Africa, Aridity, Hydroclimate, Volcanic Eruption

1. Introduction

Global climate change has intensified hydroclimatic stress worldwide, with major consequences for water availability, ecosystems, and human livelihoods. Changes in precipitation, rising temperatures, and increasing atmospheric evaporative de-

mand have disrupted the balance between water supply and demand, leading to more frequent and more intense hydrological extremes, including droughts and floods (Dong et al., 2020; Wang et al., 2021). These impacts are especially pronounced in dryland regions, where limited soil moisture (Deng et al., 2020) and strong climate variability heighten vulnerability to both natural and anthropogenic forcing (Sherwood & Fu, 2014; Huang et al., 2016; Park et al., 2018). Therefore, Africa is particularly susceptible to aridity intensification because large parts of the continent are characterized by vast drylands and depend strongly on highly variable rainfall (Pereira, 2017; Liu et al., 2020; Adeyeri, 2025), with serious consequences for agricultural productivity (Vörösmarty et al., 2005), ecosystem resilience (Feng & Fu, 2013; Huang et al., 2016), and economic stability in predominantly rain-fed systems (Lian et al., 2021).

Evidence of aridification across Africa is manifested in declining soil moisture availability and increasing vapor pressure deficit. These hydroclimatic changes have reduced surface runoff and water availability (Piemontese et al., 2019), reflecting a growing imbalance between atmospheric moisture demand and water supply (Cook et al., 2020; Deng et al., 2020). However, due to uncertainties in projections and the limited temporal span of instrumental records, integrating insights from other climate scenarios is essential for better understanding the mechanisms underlying aridity changes.

Volcanic eruptions provide a valuable natural experiment for investigating hydroclimatic variability, as stratospheric sulfate aerosols perturb the surface energy balance and large-scale atmospheric circulation (Robock, 2000; Iles & Hegerl, 2014), creating a dramatically different climate scenario. These perturbations shift the Intertropical Convergence Zone (ITCZ) and modulate monsoon systems (Colose et al., 2016; Tejedor et al., 2021), thereby influencing both precipitation and potential evapotranspiration (PET) (Zuo et al., 2019a; Zhou et al., 2024). However, most existing studies have focused primarily on precipitation responses over limited regions (Iles et al., 2013; Haywood et al., 2013; Iles & Hegerl, 2014; Zuo et al., 2019b, 2019a; Jacobson et al., 2020; Man et al., 2021; Tejedor et al., 2021; Singh et al., 2023; Villamayor et al., 2023), leaving continent-scale aridity responses poorly constrained. Besides, precipitation anomalies do not necessarily translate into changes in hydroclimatic stress, since PET responds concurrently; studies that therefore focus solely on precipitation may misrepresent hydroclimatic stress and drought susceptibility.

These knowledge gaps highlight the need for an integrated investigation providing a more hydrologically relevant evaluation of volcanic impacts on Africa. In this study, the African hydroclimatic responses to volcanic eruptions are analyzed using simulations from the Community Earth System Model Last Millennium Ensemble (CESM-LME), with assessment based on the aridity index (AI), which is defined by the ratio of precipitation to PET. Further, we quantify AI responses to Northern Hemisphere, Southern Hemisphere, and Tropical eruptions by decomposing anomalies into the relative contributions of precipitation and PET. The

remainder of this paper is structured as follows: Section 2 describes data and methods; Section 3 presents results, including characteristics of seasonal AI responses to volcanic eruptions and their associated mechanisms; and a summary and discussion are provided in Section 4.

2. Data and Methods

2.1. Data

This study utilizes monthly climate outputs from the CESM-LME, developed by the National Center for Atmospheric Research (NCAR), in which volcanic forcing is applied as a physically constrained perturbation to isolate externally forced aridity signals from internal climate variability. CESM-LME has been widely used to investigate volcanic impacts on climate, including large-scale hydroclimate and atmospheric circulation responses (Otto-Bliesner et al., 2016; Stevenson et al., 2016; Zuo et al., 2018), providing a robust foundation for analysing long-term climate responses to volcanic eruptions. The CESM-LME consists of fully coupled Earth system simulations spanning 850-2005 CE, employing CESM version 1.1 with the Community Atmospheric Model version 5 (CAM5) at a resolution of 1.9˚ × 2.5˚ (Otto-Bliesner et al., 2016).

We specifically analyze the ensemble-mean volcanic-forcing simulations, which enables robust separation of externally forced climate signals from internal variability. To characterize the hydrological response, we employ the aridity index (AI) together with total column soil moisture, defined as the vertically integrated soil water content across all modelled soil layers, and surface runoff, representing total runoff generated at the land surface and excluding subsurface drainage (Liu et al., 2021; Liu & Zhou, 2023). These variables provide complementary and physically consistent measures of land-surface hydrological responses to volcanic forcing.

2.2. Criteria for Volcano Selection

Volcanic eruptions were classified as Northern Hemisphere (NH), Southern Hemisphere (SH), or Tropical events (**Table 1**) based on the hemispheric ratio of stratospheric sulfate aerosol loading, following Stevenson et al. (2016). Only eruptions with peak total stratospheric sulfate aerosol injections exceeding the long-term mean forcing were retained, ensuring that the analysis focuses on climatically relevant events. To further enhance robustness, we restricted the selection to eruptions whose peak aerosol forcing occurred in the same season, thereby minimizing the influence of seasonal phase differences on the composite signals (Liu et al., 2016; Misios et al., 2022; Zeng & Chen, 2025).

We applied the Superposed Epoch Analysis (SEA) technique to isolate volcanic signals in the Aridity Index (AI), soil moisture, and surface runoff (Haurwitz & Brier, 1981). Seasonal anomalies for each eruption year were calculated relative to a 5-year pre-eruption climatological baseline, separately for June-July-August (JJA), September-October-November (SON), and December-January-February (DJF).

Statistical significance was evaluated using a Monte Carlo significance test, in which composite anomalies were compared against distributions generated from randomly resampled non-eruption years (Adams et al., 2003), providing a robust, non-parametric assessment of the volcanic signal relative to internal climate variability.

Table 1. List of selected volcanic events.

Class	Eruption Years
Northern (NH)	1176, 1213, 1600, 1641, 1762, and 1835
Southern (SH)	1275, 1341, and 1452
Tropical (TR)	1001, 1258, 1284, 1416, 1809, 1815, and 1991

2.3. Aridity Index

In this study, to quantify hydroclimatic responses to volcanic eruptions across Africa, we employ AI, which is widely used to represent the balance between moisture supply and atmospheric demand and, consequently, to characterize hydroclimatic dryness (Huang et al., 2016; Liu et al., 2018; Liu et al., 2019). AI is computed as the ratio of precipitation (P) to PET (Middleton & Thomas, 1997):

$$\mathrm{AI} = \frac{\mathrm{P}}{\mathrm{PET}} \tag{1}$$

PET is estimated using the FAO-56 Penman-Monteith equation (Allen et al., 1998), the standard method for quantifying atmospheric evaporative demand. The formulation integrates net radiation, air temperature, humidity, and wind speed to represent the combined radiative and aerodynamic controls on evapotranspiration and can be expressed as

$$PET = \frac{0.408\Delta\left(R_n - G\right) + \gamma \dfrac{900}{T_{mean} + 273} U_2 \left(1 - RH\right) e_s}{\Delta + \gamma\left(1 + 0.34U_2\right)} \tag{2}$$

where T_{mean}, Δ, γ, R_n, ω, and G denote monthly mean near-surface air temperature (˚C), slope of the saturation vapor pressure curve (kPa C^{-1}), psychrometric constant (kPa ˚C^{-1}), net radiation, and soil heat flux density, respectively. U_2 is 2 m wind speed (m s^{-1}) derived from the 10 m wind speed using the logarithmic wind profile conversion. e_s is the saturation vapor pressure (kPa), and e_a is the actual vapor pressure (kPa), computed from relative humidity. The term $(R_n - G)$ represents the available energy for evapotranspiration. All required variables are directly available from the CESM-LME output, ensuring consistency between PET estimates and the simulated surface energy and moisture budgets.

To assess the relative roles of precipitation and PET in driving AI changes over Arica, AI anomalies were decomposed into the contributions from precipitation and PET following the approach of Feng and Fu (2013):

$$\Delta\mathrm{AI} \approx \mathrm{F}\left(\Delta\mathrm{P}\right) + \mathrm{G}\left(\Delta\mathrm{PET}\right) \tag{3}$$

$$F(\Delta P) = \frac{\Delta P}{PET} \tag{4}$$

$$G(\Delta PET) = -\frac{P}{PET^2}\Delta PET + \frac{P}{PET^3}(\Delta PET)^2 \tag{5}$$

where $F(\Delta P)$ and $G(\Delta PET)$ represent the respective contributions of precipitation and PET anomalies to changes in AI, and ΔAI, ΔP, and ΔPET denote the changes in AI, P, and PET relative to their pre-eruption climatological means.

2.4. Moisture Budget Analysis

To elucidate the atmospheric and land-surface processes driving divergent AI responses to volcanic eruptions across Africa, we employed a moisture budget framework. This approach quantifies the contributions of moisture transport, convergence, and surface fluxes to hydroclimatic variability. Following Chou et al. (2009), we conducted a vertically integrated seasonal mean moisture budget analysis, expressed as

$$P = E - \frac{\partial}{\partial t}\langle q\rangle - \langle \nabla_h \cdot (\mathbf{V}_h q)\rangle - \langle \partial_p (q\omega)\rangle + \delta \tag{6}$$

where P, E, q, $\mathbf{V}_h$, ω, and δ denote precipitation, evaporation, specific humidity, horizontal wind vector, vertical pressure velocity, and the residual term, respectively, and $\langle\cdot\rangle$ denotes tropospheric mass integration. The residual term (δ) represents unresolved processes including data inconsistencies, subgrid-scale transport, numerical discretization errors, and imperfect budget closure.

Assuming $\omega \approx 0$ at the surface and tropopause, and neglecting moisture storage on seasonal timescales, the budget reduces to

$$P \approx E - \langle \partial_p (q\omega)\rangle - \langle \mathbf{V}_h \cdot \nabla_h q\rangle \tag{7}$$

Consequently, anomalous precipitation can be decomposed into its contributing components as

$$P' \approx E' - \langle \partial_p (q\omega)\rangle' - \langle \mathbf{V}_h \cdot \nabla_h q\rangle' + \delta \tag{8}$$

We explicitly quantified the magnitude of the residual term (δ) for all regions, seasons, and eruption categories considered. The residual was found to be small relative to the dominant moisture budget terms, precipitation, evaporation, and moisture flux convergence. In most cases, δ accounts for less than 5% - 10% of the total moisture tendency, indicating that the moisture budget closes satisfactorily at seasonal timescales.

The anomalous moisture budget terms were further decomposed into thermodynamic, dynamic, and nonlinear contributions as

$$P' = E' - \langle \bar{\omega}\partial_p q'\rangle - \langle \omega'\partial_p \bar{q}\rangle - \langle \bar{\mathrm{V}} \cdot \nabla q'\rangle - \langle \mathrm{V}' \cdot \nabla \bar{q}\rangle + NL \tag{9}$$

where overbars denote climatological means, primes denote anomalies, and NL represents nonlinear residual terms. The small magnitude of δ confirms that the diagnosed thermodynamic and dynamic components robustly explain the precip-

itation and AI responses to volcanic forcing and that the primary conclusions drawn from the moisture budget analysis are not sensitive to residual imbalances.

3. Results and Discussion

3.1. Seasonal Aridity Responses to Volcanic Eruptions

Previous studies have examined the hydroclimatic impacts of volcanic eruptions, primarily focusing on precipitation responses on a global basis (Iles et al., 2013; Iles & Hegerl, 2014; Zuo et al., 2019a; Tejedor et al., 2021; Zhou et al., 2024) and, over Africa, mainly on the Sahel and West Africa (Haywood et al., 2013; Jacobson et al., 2020). These studies have shown that volcanic aerosol forcing perturbs large-scale circulation and monsoon rainfall. However, the hydroclimatic implications of these changes have largely been interpreted through precipitation alone. As a result, the combined influence of volcanic-driven changes in moisture supply and atmospheric evaporative demand, which together control hydroclimatic stress, remains poorly constrained at the continental scale over Africa. In addition, most work has concentrated on individual seasons or single eruption events, leaving seasonal and spatial patterns of aridity largely unresolved. Extending these studies, the present analysis quantifies African hydroclimatic responses to NH, SH, and tropical volcanic eruptions from an aridity perspective. Using AI anomalies alongside soil moisture and surface runoff, we examine the spatial and seasonal variability of AI following volcanic forcing and investigate the underlying mechanisms driving these responses. All percentage changes reported below represent anomalies relative to the 5-year pre-eruption seasonal climatology (JJA, SON, DJF), normalized by that baseline.

African AI exhibits a strong seasonal sensitivity to volcanic forcing that is closely tied to the climatological position of the seasonal rainfall band and its hemispheric displacement following NH, SH, and tropical eruption events (**Figure 1**). For NH eruptions, the primary drying zone is displaced northward, aligning with the rainfall belt over the Sahel and West Africa, while regions south of the band experience compensating wetting. At the continental scale, this manifests as moderate wetting of about 6.2% during JJA, slight drying of approximately 3.7% in SON, and pronounced wetting in DJF, indicating a substantial redistribution of AI across the continent. In contrast, SH eruptions shift the dominant drying zone southward, with persistent, continent-wide drying throughout the year, strongest in SON, with continued reductions of approximately 5.2% in JJA and 3.5% in DJF. Tropical eruptions generate the weakest response, with modest drying in JJA and SON and only marginal wetting in DJF.

To diagnose the regional contributions to the continental-scale signals, Africa was subdivided into five hydroclimatic regions based on fixed latitude-longitude boundaries: North Africa (20˚N - 30˚N, 15˚W - 35˚E), the Sahel and West Africa (5˚N - 20˚N, 15˚W - 25˚E), Central Africa (5˚S - 5˚N, 10˚E - 30˚E), the Horn of Africa (5˚N - 15˚N, 35˚E - 50˚E), and Southern Africa (30˚S - 15˚S, 15˚E - 35˚E). Analysis of regional AI anomalies shows that the continental mean conceals sub-

stantial spatial heterogeneity in the hydroclimatic response to volcanic forcing (Figure 1(a)-(i)). Following NH eruptions, regional AI anomalies exhibit a pronounced meridional dipole that is tightly aligned with the climatological position of the African rainy season (Figure 1(a)-(c)). This pattern reflects a northward displacement of the primary drying zone following NH eruptions, consistent with the seasonal migration of the African rainfall belt.

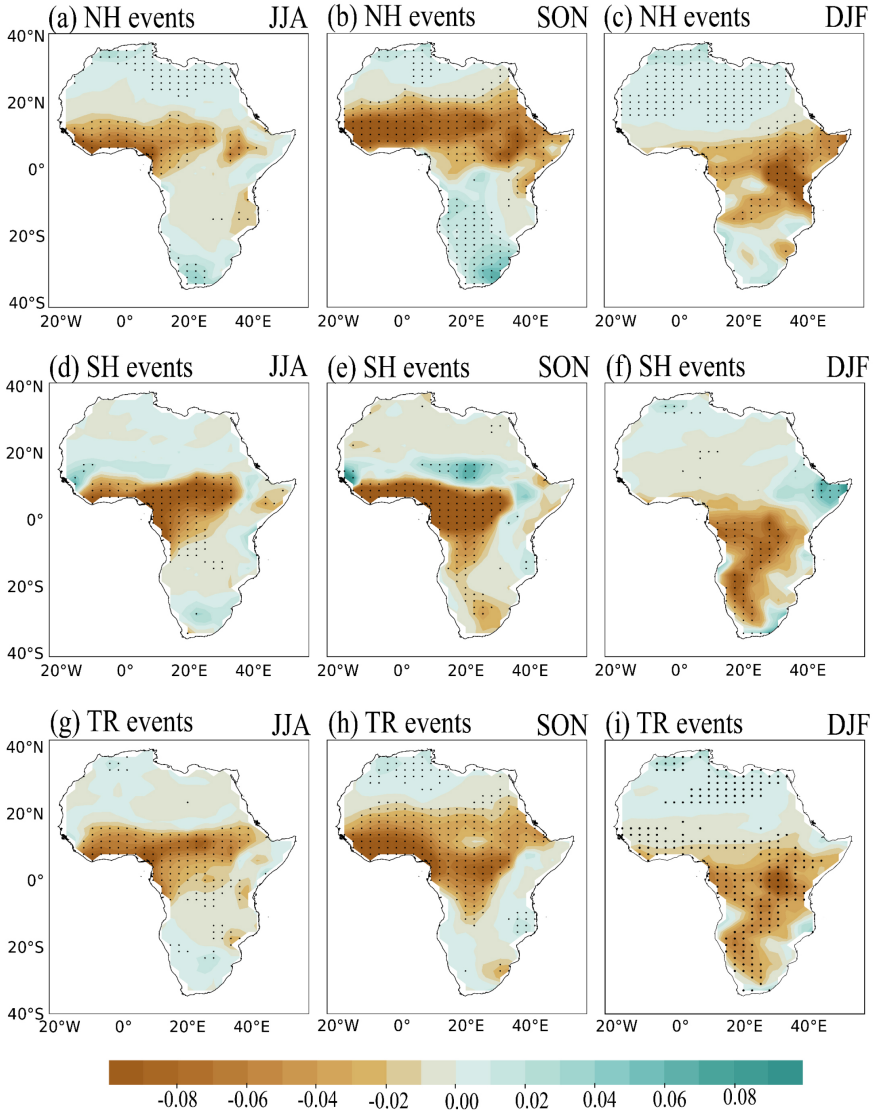

Figure 1. Seasonal AI anomalies following Northern Hemisphere (NH), Southern Hemisphere (SH), and Tropical (TR) volcanic eruptions during (a, d, g) JJA, (b, e, h) SON, and (c, f, i) DJF. Stippling denotes changes significant at the 90% confidence level.

During JJA, drying dominates the Sahel, West Africa, and Central Africa, while North Africa and Southern Africa become anomalously wetter, forming a pronounced meridional dipole aligned with the climatological rainy-season band. In SON, drying intensifies and expands across much of the continent, with reduc-

tions of 20.2% in the Sahel and West Africa, 23.2% in the Horn of Africa, and 21.9% in North Africa, while Southern Africa exhibits strong wetting of approximately 27.0%. By DJF, enhanced wetting over North Africa contrasts sharply with persistent drying over the Sahel and the Horn of Africa, reflecting a southward displacement of AI anomalies following the seasonal migration of the climatological rainfall belt.

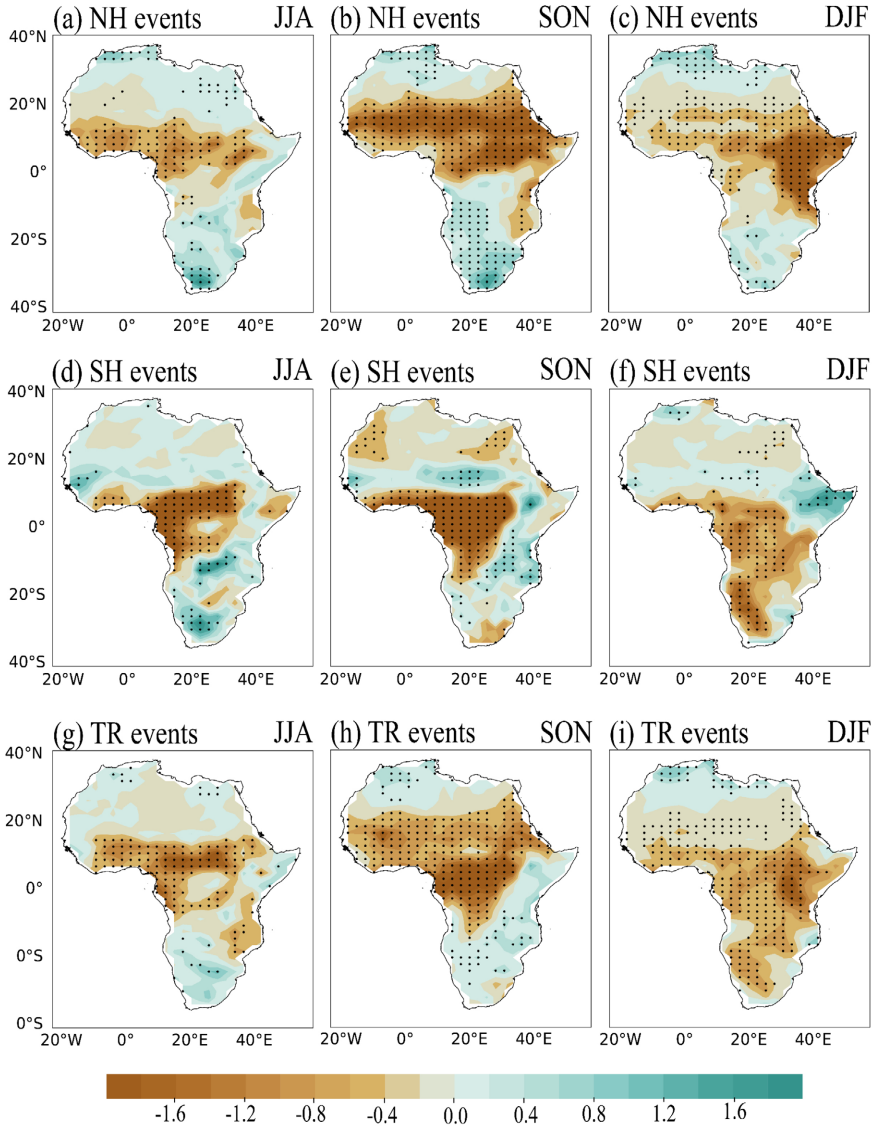

Figure 2. Seasonal soil moisture anomalies following Northern Hemisphere (NH), Southern Hemisphere (SH), and Tropical (TR) volcanic eruptions during (a, d, g) JJA, (b, e, h) SON, and (c, f, i) DJF. Stippling denotes changes significant at the 90% confidence level.

Following SH eruption events, negative AI anomalies are concentrated south of the equator and within the climatological rainy-season band during JJA and SON, indicating a southward displacement of the dominant drying zone relative to NH eruptions (Figure 1(d)-(f)). Central Africa experiences the strongest deficits in

JJA and SON, with drying extending into Southern Africa as the seasonal rainfall band migrates southward. In SON, this drying intensifies and expands, with AI reductions of up to 15.9%. Although localized wetting appears over the Horn of Africa in DJF, negative AI anomalies remain the dominant continental signal.

Tropical eruptions produce weaker but broadly coherent drying across the Sahel, Central Africa, and the Horn of Africa during JJA and SON, with reductions ranging from approximately 10% to 19%. In DJF, strong wetting emerges over North Africa, while drying persists elsewhere. Regions exhibiting statistically significant anomalies largely coincide with climatologically sensitive hydroclimatic zones, highlighting the pronounced spatial heterogeneity of African hydroclimatic responses to volcanic forcing.

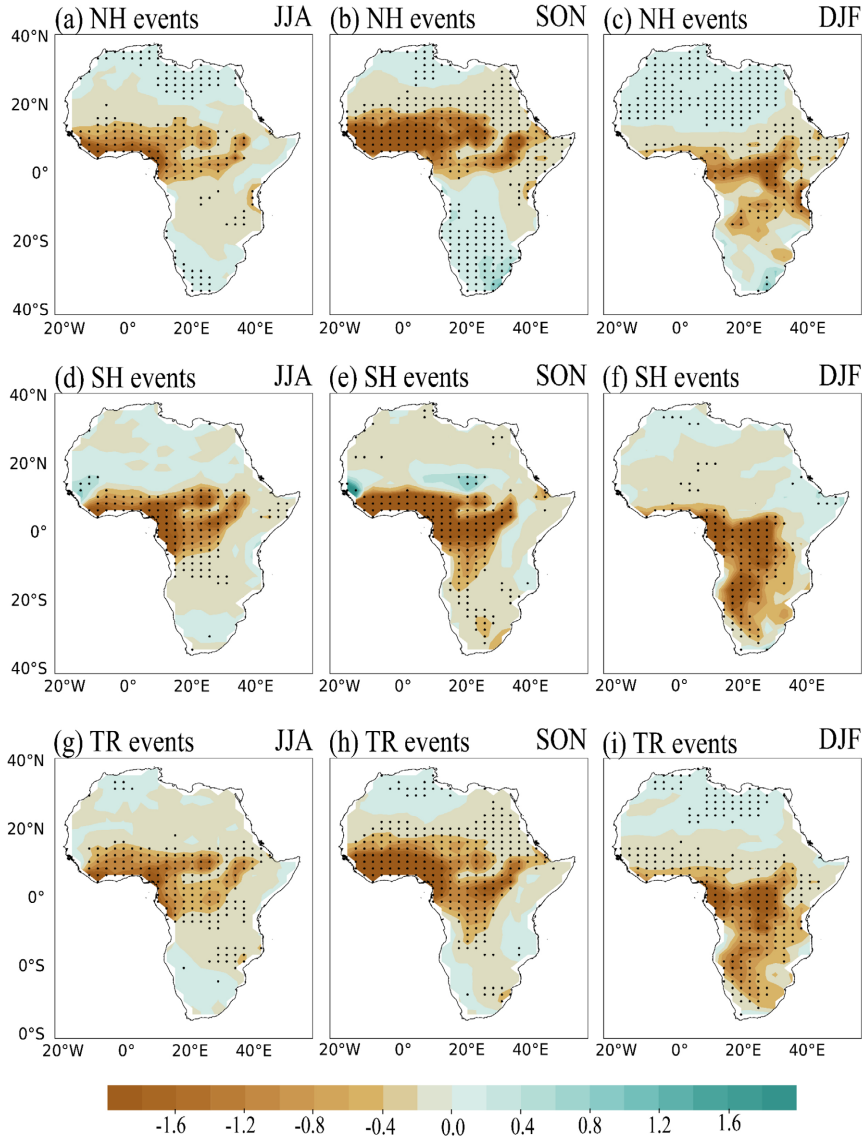

Figure 3. Seasonal surface runoff anomalies following Northern Hemisphere (NH), Southern Hemisphere (SH), and Tropical (TR) volcanic eruptions during (a, d, g) JJA, (b, e, h) SON, and (c, f, i) DJF. Stippling denotes changes significant at the 90% confidence level.

We extend the analysis to soil moisture and surface runoff (Figures 2-3) to assess terrestrial hydrological responses to volcanic eruptions. Soil moisture refers to total column soil moisture integrated across all modelled soil layers, and runoff represents total surface runoff generated at the land surface. Soil moisture and runoff deficits are strongest where seasonal rainfall normally dominates land-atmosphere coupling, reinforcing the role of rainfall-band displacement in shaping volcanic hydroclimatic impacts. Soil moisture anomalies (Figure 2) largely mirror AI patterns (Figure 1), although they exhibit more localized spatial structures. Following NH eruption events, JJA and SON show widespread deficits across Northern and Central Africa, particularly in the Sahel and West Africa, reflecting suppressed monsoonal rainfall. In contrast, Southern Africa experiences an increase of up to 1.2%. During DJF, drying shifts southward into Central and East Africa, with modest moistening in Northern Africa. SH eruptions induce more uniform soil moisture reductions across Central and Southern Africa, with limited DJF wet anomalies in the Sahel and Horn of Africa. Tropical eruptions produce weaker and more diffuse soil moisture anomalies across the Sahel, Central, and Southern Africa.

Surface runoff responds coherently (Figure 3): NH eruptions reduce runoff in the West African monsoon and equatorial regions and increase it in Southern Africa, while SH eruptions drive widespread reductions of up to 1.6% with only localized wet patches. Tropical eruptions generate modest, diffuse reductions. Statistically significant anomalies closely align with soil moisture and AI patterns, emphasizing the tight coupling between volcanic forcing, land-surface water availability, and runoff.

3.2. Contributions of Precipitation and Potential Evapotranspiration to AI Changes

In this study, the analysis further examines the relative contributions of precipitation and PET to AI changes. By isolating the individual effects of ΔP and ΔPET, we assess how each component shapes AI variability following volcanic eruption events. Across Africa, all eruption events (Figure 4) show that reductions in precipitation dominate the AI response, while ΔPET contributes only weakly and often acts to partially offset ΔP-driven anomalies. For NH eruption events (Figure 4(a)-(c) and Figure 4(j)-(l)), JJA-SON AI anomalies are driven by widespread precipitation deficits of roughly 50% across the Sahel and Northern Africa, yielding statistically robust AI reductions of approximately 36% to 48%. During DJF, these responses weaken and become more spatially fragmented.

The corresponding ΔPET anomalies are small and generally positive, reflecting volcanically induced reductions in net radiation that suppress evaporative demand, and therefore provide only a minor compensating effect, confirming that precipitation deficits are the primary driver of AI changes following NH events. In contrast, SH eruption events (Figure 4(d)-(f) and Figure 4(m)-(o)) generate a more spatially coherent signal over equatorial and Southern Africa, where precip-

itation declines of approximately 48% lead to AI decreases of 31% to 38%. In this case, ΔPET reductions play a relatively stronger but still secondary role, particularly during SON, consistent with eruption-induced radiative cooling suppressing atmospheric evaporative demand, although ΔP remains the dominant contributor in most regions.

Tropical eruption events (**Figure 4(g)-(i)** and **Figure 4(p)-(r)**) produce the largest and most spatially extensive ΔP-driven drying, with precipitation declines near 49% corresponding to AI reductions of 38% to 41%, particularly during JJA and SON, while ΔPET changes remain weak and spatially uniform, acting mainly to modestly modulate rather than control the precipitation-driven AI response. Overall, this decomposition demonstrates that African AI anomalies following volcanic eruption events are overwhelmingly precipitation-controlled, with ΔPET exerting a secondary influence that varies seasonally and hemispherically, underscoring pronounced asymmetries in the hydroclimatic response.

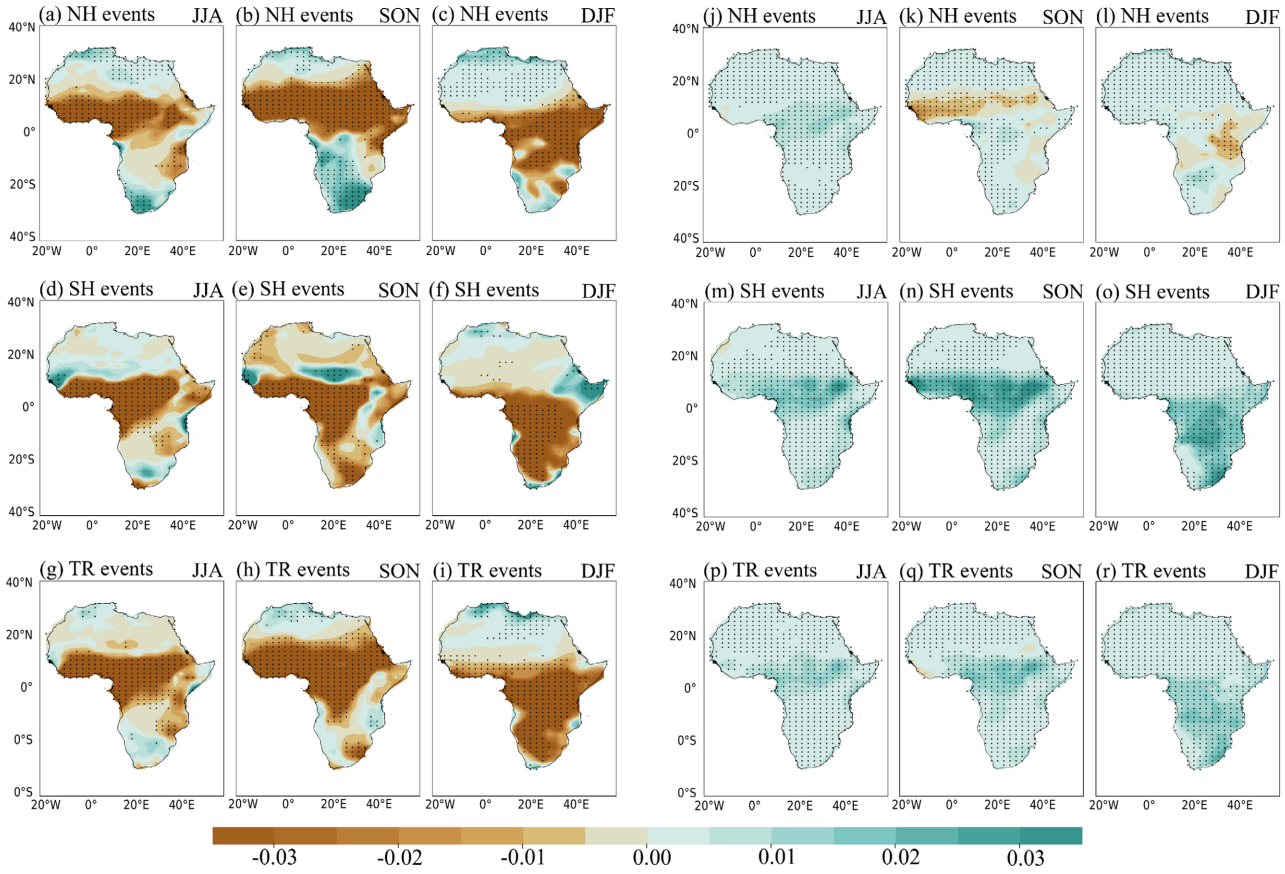

Figure 4. Contributions of ΔP (a -i) and ΔPET (j - r) to post-volcanic AI anomalies for Northern Hemisphere (a - c, j - l), Southern Hemisphere (d - f, m - o), and Tropical (g - i, p - r) eruptions. Stippling denotes changes significant at the 90% confidence level.

3.3. Physical Mechanisms behind the AI Response

Furthermore, to understand the AI responses, it is essential to examine the underlying physical drivers. Volcanic eruptions alter the atmospheric energy balance

and circulation patterns, affecting moisture transport, vertical and horizontal advection, and surface energy fluxes. Figures 5-6 highlight how these processes, particularly moisture flux convergence and wind anomalies, shape the spatial and seasonal distribution of AI responses across Africa.

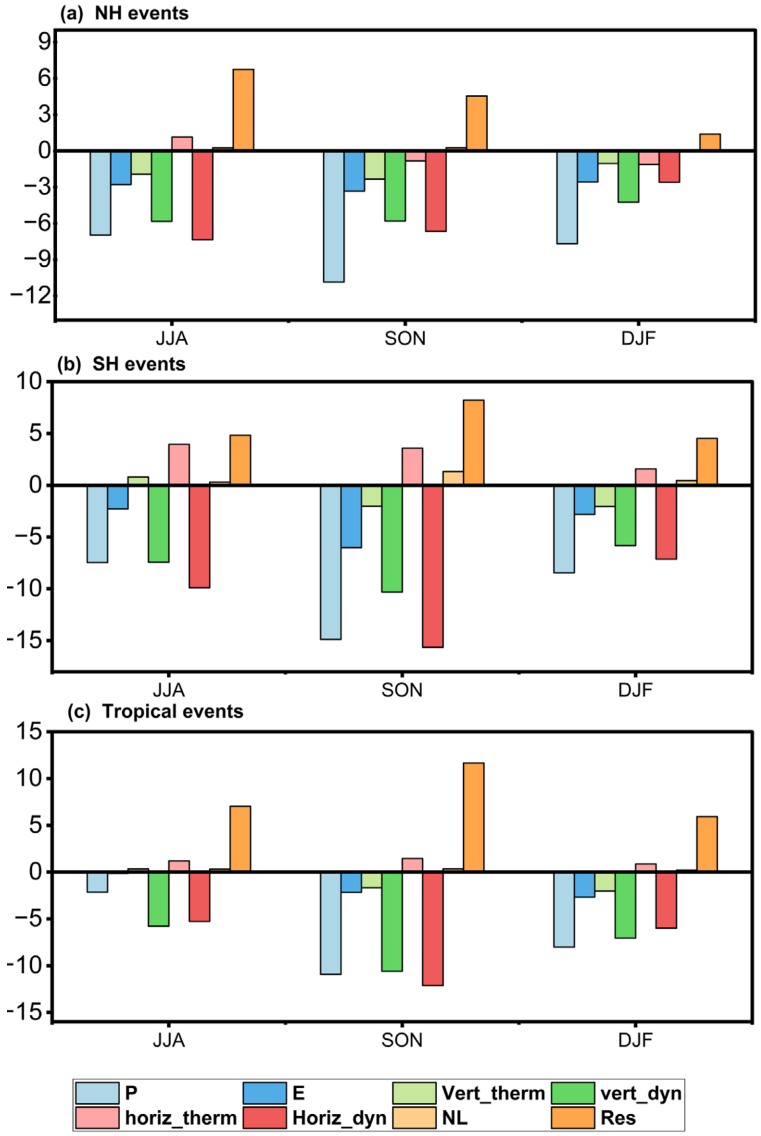

Figure 5. Seasonal moisture budget decomposition of precipitation changes over Africa following (a) Northern Hemisphere, (b) Southern Hemisphere, and (c) Tropical volcanic eruptions.

The moisture budget decomposition (Figure 5) shows that circulation-driven advection dominates precipitation changes, with evaporation playing a secondary role. The residual term (δ) is consistently small across all regions and seasons, accounting for less than 5% - 10% of the total moisture tendency, confirming that the moisture budget closes satisfactorily and that the diagnosed dynamical and thermodynamic contributions robustly explain the observed AI responses.

NH eruptions produce negative precipitation anomalies in JJA and SON, primarily driven by enhanced horizontal and vertical dynamical advection, while DJF anomalies are weaker and more spatially fragmented. SH eruptions yield the strongest responses, especially in SON, where pronounced dynamical advection drives large negative precipitation anomalies, with modest compensation from thermodynamic effects and evaporation. Tropical eruptions exhibit peak responses in SON, dominated by circulation-induced moisture export from climatological rainfall regions.

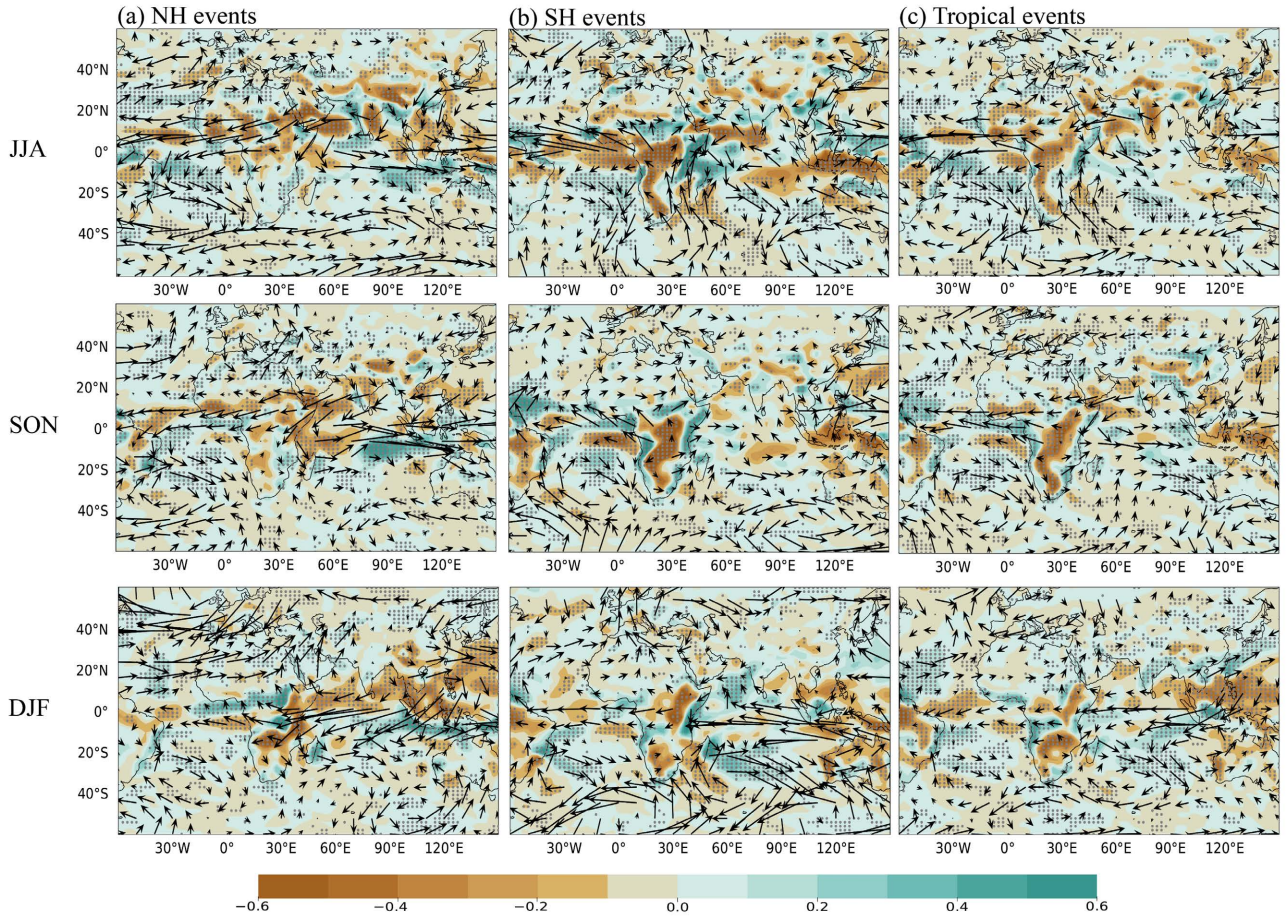

Figure 6. Seasonal anomalies of vertically integrated moisture flux divergence (shaded) and 850-hPa wind anomalies (vectors) following Northern Hemisphere (NH), Southern Hemisphere (SH), and Tropical (TR) volcanic eruptions during JJA, SON, and DJF. Stippling denotes changes significant at the 90% confidence level.

While stronger eruptions associated with higher stratospheric aerosol loading generally induce larger radiative cooling and circulation perturbations, the composite analysis employed here emphasizes the robust, large-scale AI response common across eruption events. As a result, intensity-dependent variations are partly smoothed in the composite signal. Consequently, AI anomalies are governed primarily by circulation reorganization rather than eruption magnitude alone, although individual high-intensity eruptions may locally produce stronger hydrocli-

matic responses than suggested by the composite mean.

These moisture budget decomposition results are supported by vertically integrated moisture flux divergence and 850-hPa wind anomalies (**Figure 6**), which show that regions with reduced AI (**Figure 1**) align closely with areas of enhanced moisture divergence and anomalous winds directing moisture away from Central and Southern Africa. The small magnitude of the residual term further confirms that these circulation-driven moisture transport anomalies fully account for the dominant precipitation and AI responses rather than unresolved or numerical effects.

Across all eruption categories, statistically significant AI anomalies coincide with coherent circulation changes, confirming that large-scale wind-driven moisture transport, rather than local surface fluxes, primarily controls volcanic-induced drying over the continent. Together, these circulation anomalies indicate a reorganization of large-scale moisture transport, diverting moisture away from the climatological rainfall belts and thereby explaining the observed hemispheric shifts and seasonal asymmetries in volcanic-induced African aridity.

4. Conclusion and Recommendation

Using monthly ensemble simulations from CESM-LME outputs, this study examined the quantitative hydroclimatic impacts of volcanic eruptions across Africa and their underlying mechanisms. The post-volcanic drying is not spatially uniform across Africa, but shifts with the climatological rainy-season band, with its position modulated by the eruption latitude: the dominant drying zone is displaced northward following eruptions in the Northern Hemisphere, while southward following Southern Hemisphere events, highlighting the combined effect of seasonality and volcanic eruption latitude in shaping AI responses. Soil moisture and runoff anomalies are broadly in correspondence with AI changes across all events.

Furthermore, decomposition of AI anomalies shows that precipitation reductions dominate AI changes, while PET plays a secondary role. Moisture budget analysis confirms that precipitation deficits primarily result from circulation-driven reductions in horizontal and vertical moisture advection associated with weakened large-scale ascent, which is in correspondence with previous research (Stevenson et al., 2017; Zuo et al., 2019b). Enhanced moisture flux divergence and anomalous 850-hPa winds indicate diminished moisture convergence, directly suppressing rainfall over Africa, where precipitation is strongly controlled by moisture advection, consistent with previous findings (Lélé & Leslie, 2016; Mouassom et al., 2025). Across Africa, the strong spatial correspondence between moisture flux divergence and AI reductions confirms that dynamical moisture transport changes, rather than local thermodynamic effects, govern Africa's hydroclimatic response to volcanic forcing. Overall, these results highlight the central role of large-scale atmospheric dynamics in shaping aridity responses to volcanic eruptions across Africa.

The contrasting aridity responses to NH, SH, and Tropical eruptions reflect

hemispheric asymmetries in volcanic radiative forcing and their impact on large-scale circulation. Preferential NH cooling strengthens the interhemispheric temperature gradient, displaces the ITCZ southward, and suppresses monsoonal moisture convergence (Haywood et al., 2013; Colose et al., 2016; Dogar et al., 2017), producing pronounced meridional dipoles and strong regional contrasts. In particular, the Sahel and West Africa experience marked drying during JJA and SON, while North and Southern Africa exhibit wetting, reflecting seasonal ITCZ migration. SH eruptions induce the opposite hemispheric thermal imbalance, broadly weakening cross-equatorial moisture transport and monsoon circulation, which favors widespread drying, especially over Central and Southern Africa. Tropical eruptions generate weaker, more symmetric responses, with modest drying across the Sahel, Central Africa, and the Horn of Africa and localized wetting in North Africa during DJF (Toohey et al., 2019; Zhuo et al., 2021).

These findings have direct implications for climate risk assessment and water-resource planning, as they identify moisture transport as the key control on post-eruption hydroclimatic stress. The societal relevance is the volcanic forcing integration into seasonal-to-decadal prediction systems to improve drought early-warning capabilities. Complementary priorities include evaluating model robustness across ensembles with varying monsoon and land-atmosphere representations, and refining mechanistic understanding through ITCZ, monsoon, and vertical velocity diagnostics, supported by paleoclimate reconstructions to validate modeled AI and precipitation responses.

Acknowledgements

The authors acknowledge the support of the institutions, partners, and colleagues who contributed to this study through scientific input, technical assistance, and constructive guidance. The collaborative exchanges throughout the research process helped to strengthen the analysis and improve the quality of the results presented.

Conflicts of Interest

The authors declare no conflicts of interest regarding the publication of this paper.

References

Adams, J. B., Mann, M. E., & Ammann, C. M. (2003). Proxy Evidence for an El Niño-Like Response to Volcanic Forcing. *Nature, 426,* 274-278. https://doi.org/10.1038/nature02101

Adeyeri, O. E. (2025). Hydrology and Climate Change in Africa: Contemporary Challenges, and Future Resilience Pathways. *Water, 17,* Article 2247. https://doi.org/10.3390/w17152247

Allen, R., Pereira, L., Raes, D., & Smith, M. (1998). *Crop Evapotranspiration: Guidelines for Computing Crop Water Requirements (FAO Irrigation and Drainage Paper 56).* FAO.

Chou, C., Neelin, J. D., Chen, C., & Tu, J. (2009). Evaluating the "Rich-Get-Richer" Mechanism in Tropical Precipitation Change under Global Warming. *Journal of Climate, 22,*

1982-2005. https://doi.org/10.1175/2008jcli2471.1

Colose, C. M., LeGrande, A. N., & Vuille, M. (2016). Hemispherically Asymmetric Volcanic Forcing of Tropical Hydroclimate during the Last Millennium. *Earth System Dynamics, 7,* 681-696. https://doi.org/10.5194/esd-7-681-2016

Cook, B. I., Mankin, J. S., Marvel, K., Williams, A. P., Smerdon, J. E., & Anchukaitis, K. J. (2020). Twenty-First Century Drought Projections in the CMIP6 Forcing Scenarios. *Earth's Future, 8,* e2019EF001461. https://doi.org/10.1029/2019ef001461

Deng, Y., Wang, S., Bai, X., Luo, G., Wu, L., Cao, Y. et al. (2020). Variation Trend of Global Soil Moisture and Its Cause Analysis. *Ecological Indicators, 110,* Article 105939. https://doi.org/10.1016/j.ecolind.2019.105939

Dogar, M. M., Stenchikov, G., Osipov, S., Wyman, B., & Zhao, M. (2017). Sensitivity of the Regional Climate in the Middle East and North Africa to Volcanic Perturbations. *Journal of Geophysical Research: Atmospheres, 122,* 7922-7948. https://doi.org/10.1002/2017jd026783

Dong, J., Peng, J., He, X., Corcoran, J., Qiu, S., & Wang, X. (2020). Heatwave-Induced Human Health Risk Assessment in Megacities Based on a Heat Stress-Social Vulnerability-Human Exposure Framework. *Landscape and Urban Planning, 203,* Article 103907. https://doi.org/10.1016/j.landurbplan.2020.103907

Feng, S., & Fu, Q. (2013). Expansion of Global Drylands under a Warming Climate. *Atmospheric Chemistry and Physics, 13,* 10081-10094. https://doi.org/10.5194/acp-13-10081-2013

Haurwitz, M. W., & Brier, G. W. (1981). A Critique of the Superposed Epoch Analysis Method: Its Application to Solar-Weather Relations. *Monthly Weather Review, 109,* 2074-2079. https://doi.org/10.1175/1520-0493(1981)109<2074:acotse>2.0.co;2

Haywood, J. M., Jones, A., Bellouin, N., & Stephenson, D. (2013). Asymmetric Forcing from Stratospheric Aerosols Impacts Sahelian Rainfall. *Nature Climate Change, 3,* 660-665. https://doi.org/10.1038/nclimate1857

Huang, J., Yu, H., Guan, X., Wang, G., & Guo, R. (2016). Accelerated Dryland Expansion under Climate Change. *Nature Climate Change, 6,* 166-171. https://doi.org/10.1038/nclimate2837

Iles, C. E., & Hegerl, G. C. (2014). The Global Precipitation Response to Volcanic Eruptions in the CMIP5 Models. *Environmental Research Letters, 9,* Article 104012. https://doi.org/10.1088/1748-9326/9/10/104012

Iles, C. E., Hegerl, G. C., Schurer, A. P., & Zhang, X. (2013). The Effect of Volcanic Eruptions on Global Precipitation. *Journal of Geophysical Research: Atmospheres, 118,* 8770-8786. https://doi.org/10.1002/jgrd.50678

Jacobson, T. W. P., Yang, W., Vecchi, G. A., & Horowitz, L. W. (2020). Impact of Volcanic Aerosol Hemispheric Symmetry on Sahel Rainfall. *Climate Dynamics, 55,* 1733-1758. https://doi.org/10.1007/s00382-020-05347-7

Lélé, M. I., & Leslie, L. M. (2016). Intraseasonal Variability of Low-Level Moisture Transport over West Africa. *Climate Dynamics, 47,* 3575-3591. https://doi.org/10.1007/s00382-016-3334-x

Lian, X., Piao, S., Chen, A., Huntingford, C., Fu, B., Li, L. Z. X. et al. (2021). Multifaceted Characteristics of Dryland Aridity Changes in a Warming World. *Nature Reviews Earth & Environment, 2,* 232-250. https://doi.org/10.1038/s43017-021-00144-0

Liu, F., Chai, J., Wang, B., Liu, J., Zhang, X., & Wang, Z. (2016). Global Monsoon Precipitation Responses to Large Volcanic Eruptions. *Scientific Reports, 6,* Article No. 24331. https://doi.org/10.1038/srep24331

Liu, L., Gudmundsson, L., & Seneviratne, S. I. (2020). Ecosystem Production Response to Climate Variability Globally. *Nature Communications, 11,* 1-9.

Liu, S., & Zhou, X. (2023). The PMIP4 Simulated Dryland Aridity Changes during the Last Interglacial. *Environmental Research Letters, 18,* Article 094056. https://doi.org/10.1088/1748-9326/acf725

Liu, S., Jiang, D., & Lang, X. (2018). A Multi-Model Analysis of Moisture Changes during the Last Glacial Maximum. *Quaternary Science Reviews, 191,* 363-377. https://doi.org/10.1016/j.quascirev.2018.05.029

Liu, S., Jiang, D., & Lang, X. (2019). Mid-holocene Drylands: A Multi-Model Analysis Using Paleoclimate Modelling Intercomparison Project Phase III (PMIP3) Simulations. *The Holocene, 29,* 1425-1438. https://doi.org/10.1177/0959683619854512

Liu, S., Lang, X., & Jiang, D. (2021). Time-Varying Responses of Dryland Aridity to External Forcings over the Last 21 Ka. *Quaternary Science Reviews, 262,* Article 106989. https://doi.org/10.1016/j.quascirev.2021.106989

Man, W., Zuo, M., Zhou, T., Fasullo, J. T., Bethke, I., Chen, X. et al. (2021). Potential Influences of Volcanic Eruptions on Future Global Land Monsoon Precipitation Changes. *Earth's Future, 9,* 1-14. https://doi.org/10.1029/2020ef001803

Middleton, N. J., & Thomas, D. S. G. (1997). *World Atlas of Desertification.* Arnold.

Misios, S., Logothetis, I., Knudsen, M. F., Karoff, C., Amiridis, V., & Tourpali, K. (2022). Decline in Etesian Winds after Large Volcanic Eruptions in the Last Millennium. *Weather and Climate Dynamics, 3,* 811-823. https://doi.org/10.5194/wcd-3-811-2022

Mouassom, F. L., Tamoffo, A. T., & Cardoso-Bihlo, E. (2025). Convolutional Neural Network-Based Insights into Extreme Precipitation Regional Dynamics over Central Africa Using Moisture Flux Patterns. *Journal of Geophysical Research: Atmospheres, 130,* e2025JD044341. https://doi.org/10.1029/2025jd044341

Otto-Bliesner, B. L., Brady, E. C., Fasullo, J., Jahn, A., Landrum, L., Stevenson, S. et al. (2016). Climate Variability and Change since 850 CE: An Ensemble Approach with the Community Earth System Model. *Bulletin of the American Meteorological Society, 97,* 735-754. https://doi.org/10.1175/bams-d-14-00233.1

Park, C., Jeong, S., Joshi, M., Osborn, T. J., Ho, C., Piao, S. et al. (2018). Keeping Global Warming within 1.5˚C Constrains Emergence of Aridification. *Nature Climate Change, 8,* 70-74. https://doi.org/10.1038/s41558-017-0034-4

Pereira, L. (2017). *Climate Change Impacts on Agriculture Across Africa.* Oxford University Press.

Piemontese, L., Fetzer, I., Rockström, J., & Jaramillo, F. (2019). Future Hydroclimatic Impacts on Africa: Beyond the Paris Agreement. *Earth's Future, 7,* 748-761. https://doi.org/10.1029/2019EF001169

Robock, A. (2000). Volcanic Eruptions and Climate. *Reviews of Geophysics, 38,* 191-219. https://doi.org/10.1029/1998rg000054

Sherwood, S., & Fu, Q. (2014). A Drier Future? *Science, 343,* 737-739. https://doi.org/10.1126/science.1247620

Singh, R., Tsigaridis, K., LeGrande, A. N., Ludlow, F., & Manning, J. G. (2023). Investigating Hydroclimatic Impacts of the 168-158 BCE Volcanic Quartet and Their Relevance to the Nile River Basin and Egyptian History. *Climate of the Past, 19,* 249-275. https://doi.org/10.5194/cp-19-249-2023

Stevenson, S., Fasullo, J. T., Otto-Bliesner, B. L., Tomas, R. A., & Gao, C. (2017). Role of Eruption Season in Reconciling Model and Proxy Responses to Tropical Volcanism. *Proceedings of the National Academy of Sciences, 114,* 1822-1826.

https://doi.org/10.1073/pnas.1612505114

Stevenson, S., Otto-Bliesner, B., Fasullo, J., & Brady, E. (2016). "El Niño Like" Hydroclimate Responses to Last Millennium Volcanic Eruptions. *Journal of Climate, 29,* 2907-2921. https://doi.org/10.1175/jcli-d-15-0239.1

Tejedor, E., Steiger, N. J., Smerdon, J. E., Serrano-Notivoli, R., & Vuille, M. (2021). Global Hydroclimatic Response to Tropical Volcanic Eruptions over the Last Millennium. *Proceedings of the National Academy of Sciences, 118,* e2019145118. https://doi.org/10.1073/pnas.2019145118

Toohey, M., Krüger, K., Schmidt, H., Timmreck, C., & Sigl, M. (2019). Extratropical Explosive Volcanic Eruptions. *Nature Geoscience, 12,* 1-9.

Villamayor, J., Khodri, M., Fang, S., Jungclaus, J. H., Timmreck, C., & Zanchettin, D. (2023). Sahel Droughts Induced by Large Volcanic Eruptions over the Last Millennium in Pmip4/Past1000 Simulations. *Geophysical Research Letters, 50,* e2022GL101478. https://doi.org/10.1029/2022gl101478

Vörösmarty, C. J., Douglas, E. M., Green, P. A., & Revenga, C. (2005). Geospatial Indicators of Emerging Water Stress: An Application to Africa. *AMBIO: A Journal of the Human Environment, 34,* 230-236. https://doi.org/10.1579/0044-7447-34.3.230

Wang, X., Jiang, D., & Lang, X. (2021). Future Changes in Aridity Index at Two and Four Degrees of Global Warming above Preindustrial Levels. *International Journal of Climatology, 41,* 278-294. https://doi.org/10.1002/joc.6620

Zeng, Q., & Chen, S. (2025). Different Climate Responses to Northern, Tropical, and Southern Volcanic Eruptions in CMIP6 Models. *Climate, 14,* Article 8. https://doi.org/10.3390/cli14010008

Zhou, S., Liu, F., Dai, A., & Zhao, T. (2024). Dryland Hydroclimatic Response to Large Tropical Volcanic Eruptions during the Last Millennium. *npj Climate and Atmospheric Science, 7,* Article No. 85. https://doi.org/10.1038/s41612-024-00636-y

Zhuo, Z., Kirchner, I., Pfahl, S., & Cubasch, U. (2021). Climate Impact of Volcanic Eruptions: The Sensitivity to Eruption Season and Latitude in MPI-ESM Ensemble Experiments. *Atmospheric Chemistry and Physics, 21,* 13425-13442. https://doi.org/10.5194/acp-21-13425-2021

Zuo, M., Man, W., Zhou, T., & Guo, Z. (2018). Different Impacts of Northern, Tropical, and Southern Volcanic Eruptions on the Tropical Pacific SST in the Last Millennium. *Journal of Climate, 31,* 6729-6744. https://doi.org/10.1175/jcli-d-17-0571.1

Zuo, M., Zhou, T., & Man, W. (2019a). Hydroclimate Responses over Global Monsoon Regions Following Volcanic Eruptions at Different Latitudes. *Journal of Climate, 32,* 4367-4385. https://doi.org/10.1175/jcli-d-18-0707.1

Zuo, M., Zhou, T., & Man, W. (2019b). Wetter Global Arid Regions Driven by Volcanic Eruptions. *Journal of Geophysical Research: Atmospheres, 124,* 13648-13662. https://doi.org/10.1029/2019jd031171